American Mineralogist, Volume 87, pages 1321–1332, 2002

Evolution of local electronic structure in alabandite and niningerite solid solutions [(Mn,Fe)S, (Mg,Mn)S, (Mg,Fe)S] using sulfur *K*- and *L*-edge XANES spectroscopy

SHANNON P. FARRELL,[1] MICHAEL E. FLEET,[1] ILIA E. STEKHIN,[2] ANTONINA KRAVTSOVA,[2]
ALEXANDER V. SOLDATOV,[2] AND XIAOYANG LIU[1]

[1]Department of Earth Sciences,University of Western Ontario,London, Ontario N6A 5B7, Canada
[2]Faculty of Physics, Rostov State University,344090, Rostov-on-Don, Russia

ABSTRACT

Synchrotron radiation S *K*- and *L*-edge X-ray absorption near-edge structure (XANES) spectra are reported for the cubic, rocksalt (B1) structure sulfides niningerite (MgS), alabandite (MnS), and oldhamite (CaS), and for their solid solutions (Mn,Fe)S and (Mg,Mn)S, and S *L*-edge XANES spectra are reported also for (Mg,Fe)S solid solutions. Pre-edge features at the S *K*-edge are attributed to transition of S 1*s* electrons to the lowest available unoccupied S 3*p* σ* antibonding states hybridized with metal $3d(e_g)$ states, and at the S *L*-edge to transition of S 2*p* electrons to unoccupied S 3*s* σ*, 4*s* σ*, and 3*d* antibonding states hybridized with metal $3d(e_g)$ states, and to a lesser extent $3d(t_{2g})$ states.

The S *K*-edge XANES spectra for the solid solutions show a progressive participation of 3*d* orbitals in metal-S bonding with increase in substitution by Fe in (Mn,Fe)S and (Mg,Fe)S and Mn in (Mg,Mn)S through progressive increase in the area of the pre-edge feature. However, the pre-peak area does not increase linearly in each solid solution series showing that a real change in bulk electronic properties has occurred. Increase in pre-peak area reflects an increase in overall attainability of metal 3*d* states for hybridization with S 3*p* σ* antibonding states as proportionally more metal 3*d* orbitals become available. The S *L*-edge XANES spectra show progressive evolution of pre-edge features at the L_3- and L_2-edges (a_1 and a_2, respectively). Only a_2 is present in the S *L*-edge XANES spectrum of FeS (troilite), and with progressive decrease in Fe content in (Mn,Fe)S and (Mg,Fe)S solid solutions, a_1 first appears, then becomes dominant. Since a_1 is attributed to transition of S $2p_{3/2}$ electrons to S 3*s* σ* states hybridized with metal $3d(e_g)$ and $3d(t_{2g})$ states, this appears to represent an increased contribution from metal-S π-bonding. The results show that the size and position of the pre-edge features to the S *K*- and *L*-edges are controlled more by the DOS of hybridized $3d(e_g^\beta)$ and $3d(t_{2g}^\beta)$ states and nearest-neighbor coordination of the metal atoms than by the precise coordination of S and the extended structure of the sulfide.

The full multiple scattering approach has been applied to the calculation of the S *K*-edge XANES spectra of MgS, MnS, and CaS. Results are consistent with experimental XANES spectra, especially for the pre-edge features, which are often neglected in such calculations.

INTRODUCTION

The monosulfides of Mn, Mg, Fe, and Ca with the rocksalt (B1) structure occur as alabandite (MnS), niningerite [(Mg, Fe, Mn)S], and oldhamite (CaS) in EH enstatite chondrite meteorites, where they appear to result from metamorphism under very reduced conditions (e.g., Fleet and MacRae 1987). Troilite, FeS with a derivative NiAs-type (B8) structure, is a nearly ubiquitous phase in most meteorites (Goodrich and Delaney 2000) and is the iron sulfide of lunar rocks (Frondel 1975). Alabandite also occurs in low-temperature vein deposits in the Earth's crust, and troilite occurs sporadically in magmatic sulfide assemblages of mafic/ultramafic rocks. The scientific and technological significance of the metal monosulfides has stimulated much interest due to the large diversity of physical properties related to their energy band structure. In particular, alkaline-earth chalcogenides (AECs) have applications in optical and electroptical devices and are used as phosphors. More generally, the electronic structure and bonding of metal sulfides, in both the bulk and near surface, has important implications for mineral deposits and surficial geochemistry. Their electrical and magnetic properties are strongly influenced by covalence of the metal-S bond, which results in hybridization of compatible S 3*p* and metal 3*d* bonding states and direct or indirect metal-metal bonding interactions in favorable cases. The electronic structure of the valence band (VB) of many monosulfides is well understood based on band structure and molecular orbital (MO) calculations, and on chemical spectroscopic techniques [e.g., optical spectroscopy, X-ray photoelectron spectroscopy (XPS), and X-ray emission spectroscopy (XES)]. In contrast, the electronic structure of the conduction band (CB) has received much less attention due to limitations of theoretical calculations and experimental approaches.

Synchrotron radiation (SR) X-ray absorption spectroscopy (XAS) is now a familiar tool for investigation of local struc-

---

* E-mail: Shannon.Farrell@drdc-rddc.gc.ca

0003-004X/02/0010–1321$05.00

ture and chemical state in metal sulfides, including NiAs-type, rocksalt, pyrite/marcasite, and zincblende/wurtzite phases (Sugiura and Muramatsu 1985; Kitamura et al. 1988; Li et al. 1995; Womes et al. 1997; Farrell and Fleet 2000, 2001). In particular, the X-ray absorption near-edge structure (XANES) region yields information on the lower part of the conduction band. The most prominent feature in the XANES spectrum, the absorption edge, is attributed to transition of core electrons to the lowest unoccupied antibonding states as restricted by the quantum selection rules, $\Delta L = \pm 1$, $\Delta J = 0$ or ± 1 (Azároff 1968). Transition to unoccupied nonbonding states (e.g., $3d$ states of transition-metal sulfides for S *K*-edge studies) is forbidden by the atomic selection rules in the electric dipole approximation ($\Delta L = \pm 1$). However, since electronic transitions are sensitive to stereochemical factors that change the $3d$ orbital splittings and populations, these forbidden transitions become weakly to strongly allowed at both the metal and the S *K*- and *L*-edge of metal sulfides through hybridization of S antibonding and metal $3d$ states (Tossell 1977). This *p-d* hybridization is particularly strong for $3d(e_g)$ states in NiAs-type Fe-Co-Ni monosulfides, and is associated with a prominent pre-edge feature to the absorption edge feature of S *K*-edge XANES spectra (cf. Fig. 4; Farrell and Fleet 2001). More specifically, the pre-edge feature at the S *K*-edge has been assigned to transition of S $1s$ electrons to unoccupied hybridized S $3p$ σ^* antibonding and metal $3d(e_g)$ states. The quantum selection rules permit transitions at the *L*-edge to both $3d(e_g)$ and $3d(t_{2g})$ states, but S *L*-edge studies of compounds with the NiAs-type and rocksalt structures have been limited, due to difficulties associated with surface contamination and interpretation.

Here we investigate the S *K*- and *L*-edge XANES spectra of solid solutions of transition-metal and alkaline earth monosulfides with the rocksalt structure, and use them to deduce electronic structure at the bottom of the conduction band in these materials. Also, the S *K*-edge XANES spectra of the end-member phases are reproduced by full multiple-scattering analysis, using theoretical methods first developed for early work on metal sulfides (Bianconi 1989).

EXPERIMENTAL METHODS

All samples were prepared from high-purity elements by dry reaction within evacuated sealed silica glass tubes. CaS was prepared by direct reaction of crushed Ca metal and S, weighed to excess of the stoichiometric proportion, at 600 °C overnight, followed by heating at 800 °C for 1 hour. The product was then ground and reloaded with excess S into a 20 cm long sealed silica glass tube, and heated in a horizontal tube furnace at 700 °C overnight, followed by heating at 800 °C for 1 hour, maintaining a thermal gradient along the tube sufficient to allow any excess S to condense at the cool end. The CaS product was then reacted at 1000 °C for 3 days, then ground and annealed at 1000 °C for 4 days, reground and annealed at 1000 °C for 1 hour, and quenched in water. MgS was prepared by direct reaction of Mg powder and S, weighed to a slight excess (~1 wt%) of the stoichiometric proportion, contained in a 6 mm diameter alumina crucible that was set on a graphite pedestal within a sealed silica glass tube, and heated in a vertical tube furnace at 450 °C overnight, followed by heating at 600 °C for 1 day, then at 700 °C for 1 day, and then at 800 °C for 1 hour. The MgS product was then reground, similarly loaded in a sealed silica glass tube with a slight excess (~1 wt%) of S and then heated in the presence of graphite at 600 °C for 2 hours, followed by heating at 900 °C for 2 hours, and then at 1000 °C for 3 days. MnS was prepared by direct reaction of hydrogen-reduced (~800 °C) Mn powder and S, weighed to a slight excess of ~1 wt%, at 450 °C overnight, followed by heating at 600 °C for 2 days, and then at 700 °C for 1 hour. Stoichiometric FeS (troilite) was prepared similarly by direct reaction of hydrogen-reduced (~900 °C) Fe sponge and a stoichiometric proportion of S at 450 °C overnight, followed by heating at 600 °C for 1 day, and then at 700 °C for 2 days.

Solid solutions of the metal monosulfides (Table 1) were prepared from dry mixes of appropriate molar proportions of MgS, MnS, and FeS contained in sealed silica glass tubes and reacted initially at 1000 °C for 3 days then air cooled. The products were then ground and annealed at 1000 °C for 6 days. Most charges were then quenched directly in water. However, four Fe-rich preparations ($\mathrm{Mg}_{1-x}\mathrm{Fe}_x\mathrm{S}$, $x = 1.00$ and 0.875, and $\mathrm{Mn}_{1-x}\mathrm{Fe}_x\mathrm{S}$, $x = 0.875$ and 0.750), which were extensively imbricated with the wall of the glass tube, were cooled in air, retubed, annealed at 1000 °C for 1.5 hours, and then quenched in water.

Samples were prepared in two batches using similar procedures. The first batch of samples was used for the S *K*-edge XANES study in 1999–2000. A second batch was prepared for S *L*-edge XANES and powder X-ray diffraction (P-XRD; Table

TABLE 1. Unit-cell parameter and pre-edge of the S *K*-edge XANES spectra for (Mg,Mn)S, (Mn,Fe)S, and (Mg,Fe)S solid solutions

Nominal composition			P-XRD		Pre-edge feature a	
Mg	Mn	Fe	phases present	*a* (Å)	energy (eV)	area (%)*
1.000	0.000	0.000	B1	5.2004(7)	— —	0.0
0.875	0.125	0.000	B1	5.2060(3)	2470.96	7.6
0.750	0.250	0.000	B1	5.2098(4)	2470.99	14.3
0.625	0.375	0.000	B1	5.2133(3)	2470.97	20.0
0.500	0.500	0.000	B1	5.2165(5)	2471.01	23.5
0.375	0.625	0.000	B1	5.2177(9)	2470.99	27.6
0.250	0.750	0.000	B1	5.2210(5)	2471.00	31.8
0.125	0.875	0.000	B1	5.2229(15)	2471.00	32.6
0.000	1.000	0.000	B1	5.2233(5)	2471.00	34.3
0.916	0.000	0.084	B1		2470.73	14.9
0.875	0.000	0.125	B1	5.1874(4)	— —	— —
0.833	0.000	0.167	B1		2470.55	22.5
0.750	0.000	0.250	B1	5.1720(5)	2470.35	27.7
0.625	0.000	0.375	B1	5.1557(5)	— —	— —
0.500	0.000	0.500	B1 †	5.1385(4)	2470.20	46.4
0.375	0.000	0.625	B1 †	5.1204(3)	2470.16	53.4
0.250	0.000	0.750	B1 + B8	5.1129(5)	2470.06	63.2
0.125	0.000	0.875	B8 + B1	5.1099(5)	2469.92	87.4
0.000	0.000	1.000	B8‡	— —	2469.89	100.0
0.000	0.875	0.125	B1	5.2059(8)	2471.00	34.3
0.000	0.750	0.250	B1	5.1872(3)	2470.85	38.7
0.000	0.625	0.375	B1	5.1636(8)	2470.73	43.4
0.000	0.500	0.500	B1	5.1421(8)	2470.60	46.3
0.000	0.375	0.625	B1 †	5.1189(9)	2470.48	50.7
0.000	0.250	0.750	B1 + B8	5.0993(2)	2470.37	55.6
0.000	0.125	0.875	B8 + B1	5.0944(4)	2470.15	69.7

Notes: Energies are calibrated relative to the S *K*-edge peak of native S at 2472.0 eV.

* Normalized to 100% for the area of the pre-peak in the S *K*-edge XANES spectrum of FeS (troilite; B8).

† Contains trace quench FeS (troilite).

‡ The B8 phase is FeS (troilite) with $a = 5.9667(15)$ Å and $c = 11.7516(29)$ Å.

1, Fig. 1). Sulfur *K*-edge XANES spectra were collected for a selection of samples from the second batch and gave results in excellent agreement with the earlier measurements. P-XRD diffractograms were collected with a Rigaku X-ray diffractometer equipped with a Co rotating anode source operating at 45 kV, 160 mA, with automated removal of the Co$K\alpha_2$ peak and peak position determination; the Co$K\alpha_1$ wavelength used was 1.788965 Å. All powder patterns were collected over a range of 25 to 120° 2θ, which included all reflections up to 422 of the B1 phase, with a step size of 0.02° 2θ, and were calibrated using silicon [JCPDS-ICDD no. 27-1402; a = 5.43088(4) Å] as an internal standard.

Sulfur *K*- and *L*-edge XANES spectra were collected at the Canadian Synchrotron Radiation Facility (CSRF), Aladdin storage ring (University of Wisconsin at Madison, Wisconsin). The storage ring operates at either 800 MeV or 1 GeV with a ring current of 60–180 mA or 40–80 mA, respectively; XANES spectra were not markedly affected by differences in operating energy. The S *K*- and *L*-edge spectra were measured on a double crystal monochromator (DCM) beamline and a Mark IV Grasshopper monochromator beamline, respectively, in both total electron yield (TEY) and fluorescence yield (FY) modes as a function of incident photon energy (Bancroft 1992); both beamlines actually collect the current yield (CY) but this has traditionally been referred to as "TEY." The DCM is described by Yang et al. (1992) and uses an InSb (111) crystal; it has an energy resolution of about 0.6 eV (FWHM) at 1840 eV, and the Darwin width of the crystal corresponds to an energy resolution of 0.9 eV for the S *K*-edge. The Grasshopper beamline is described by Tan et al. (1982) and uses an 1800/mm holographic grating with an energy resolution of <0.1 eV in the S *L*-edge region. The superior resolution at the S *L*-edge is attributed to inherently narrower natural linewidths and narrower photon widths due to use of a low energy grazing incidence monochromator, rather than a crystal monochromator.

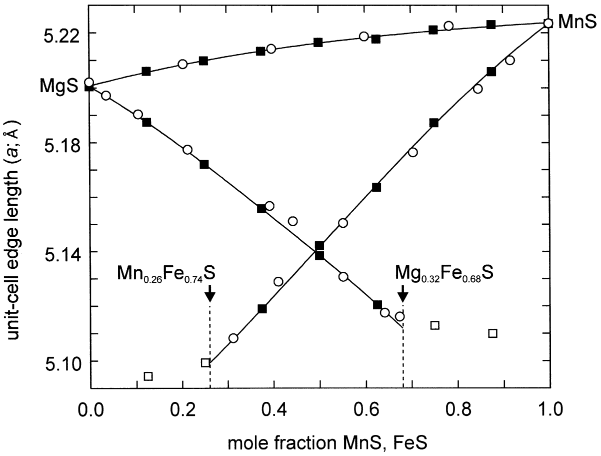

FIGURE 1. Variation of the a unit-cell parameter (Å) with composition for binary (Mn,Fe)S, (Mg,Mn)S, and (Mg,Fe)S solid solutions (full squares) compared with results of Skinner and Luce (1971; open circles). The solvus for rocksalt structure $Mn_{1-x}Fe_xS$ and $Mg_{1-x}Fe_xS$ is at 26 mol% MnS and 68 mol% FeS, respectively, and open squares are results for bulk compositions yielding rocksalt (B1) phase coexisting with FeS (B8).

The TEY recording mode probes the near surface (estimated at <200 Å depth for the S K edge and <50 Å depth for the S *L*-edge) and is sensitive to near-surface impurities and alteration, whereas the FY mode is more representative of the bulk material (i.e., >1000 Å depth for the S K edge and ~600 Å depth for the S *L* edge; Kawai et al. 1994; Kasrai et al. 1996). Thus, collection of spectra in both the TEY and FY modes simultaneously for the same sample, particularly for the *L*-edge, provides information on near-surface homogeneity and structural continuity. Transmission measurements have not been made in the XANES region on the DCM or Grasshopper beamlines. For XANES spectroscopy, differences between TEY and FY modes are attributed to bulk sensitivity and scaling only. However, for EXAFS spectroscopy, which is not presently investigated, differences in amplitude between TEY and FY modes can introduce small differences in measured bond lengths (Stöhr 1988).

The grain size of the samples was <0.3 mm in diameter; therefore, individual crystals were too small to cleave. For both *K*- and *L*-edge studies, the sample was crumbled, if necessary, but not ground, and uniformly distributed on double-sided conducting carbon tape affixed to a clean stainless steel disk. For the *K*-edge XANES spectra, the sealed silica glass sample tubes were opened in air immediately before measurement. However, the relatively high reactivity of the metal sulfides and the near-surface sensitivity of the *L*-edge measurements made it essential to collect the *L*-edge spectra on samples with minimal exposure to air and moisture. Therefore, for *L*-edge measurements, sample preparation, including opening of the sample tubes, and transfer into the experimental chamber of the Grasshopper was performed in a nitrogen-filled glove bag attached to the port of the spectrometer sample chamber.

DCM (*K*-edge) measurement conditions included a photon energy range of 2450–2525 eV at a step size of 0.25 eV, with count times determined by counting statistics (~3.3 s per step), and 2 scans per sample, giving a total run time of approximately 27 minutes per sample. Normalization at the *K*-edge was unnecessary as collection times for *K*-edge spectra were determined by counting statistics, which effectively accounts for variations in I_o. The Grasshopper (*L*-edge) measurement conditions included a photon energy range of 155–190 eV at a step size of 0.07 eV, with a count time of 1 s per step and 4 scans per sample, giving a total run time of approximately 40 minutes per sample. *L*-edge spectra were normalized against incident intensity (I_o), which was measured simultaneously. Both TEY and FY modes of *L*-edge spectra yielded similar spectral features, but the TEY spectra are presently used for presentation and interpretation due to their more favorable signal-to-noise ratio. Data reduction and analysis used the BAN and BGAUSS data analysis programs (Tyliszcak 1992), and FORTRAN77 codes. All spectra were calibrated to the *K*- or L_3-edge peak of native S at 2472.0 eV and 162.5 eV ($2p_{3/2}$; Fuggle and Inglesfield 1992; Weast et al. 1986), respectively, after removal of a linear pre-edge background. To discern relative changes in subtle XANES features, all spectra were scaled relative to the maximum peak height at the edge. S *K*- and *L*-edge spectra for native S were collected at the beginning of each beam time session for calibration purposes and showed excellent agreement with respect to relative position and intensity of spectral features.

ELECTRONIC STRUCTURE OF END-MEMBERS

Manganese monosulfide, MgS, and CaS crystallize with the rocksalt (B1) structure (space group $Fm\overline{3}m$ and have metal and S atoms in octahedral coordination with nearest neighbors. Iron monosulfide (FeS; troilite) has a derivative NiAs-type (B8) structure (space group $P6_3/mmc$) in which Fe and S atoms are also in sixfold coordination with nearest neighbors but, although Fe remains in octahedral coordination with S, S is in trigonal prismatic coordination with Fe. The structure of troilite is a superstructure of the NiAs-type structure with unit-cell parameters $A\sqrt{3}$ and $2C$, where A and C refer to the NiAs subcell. A key feature of the NiAs-type structure is the sharing of MS_6 octahedral faces, which permits a metal-metal bonding interaction along the **c** direction through hybridization of either $3d(t_{2g})$ or $3d(e_g)$ orbitals. The rocksalt and NiAs-type structures are compared in Figure 1 of Farrell and Fleet (2000).

The alkaline earth chalcogenides (AECs) are considered to be insulators or large band gap semiconductors; band structure schematics are given in Figure 2. Divalent Mg differs from Ca, Mn, and Fe in that there are no metal 3*d* orbitals in the band gap available for hybridization with S 3*p* orbitals. At room temperature and pressure, both MgS and CaS are diamagnetic and classical insulators or large indirect ($\Gamma - X$) band gap semiconductors (Stepanyuk et al. 1989, 1992). In materials with an indirect band gap the bottom of the conduction-band (CB) and the top of the valence-band (VB) lie at different wavevectors. The existence of an indirect band gap at lower energy than the direct gap in MgS and CaS has important implications for absorption studies. The band gap (2.7 eV) in MgS is bounded by S 3*p* bonding orbitals in the upper part of the valence-band (VB) and by Mg 3*s* σ* (and to a lesser extent, S 3*d*) antibonding orbitals in the lower part of the conduction-band (CB) (Stepanyuk et al. 1992; Lichanot et al. 1994; Kalpana et al. 1996). In CaS, the band gap (given variously as 4.434 eV or 2.143 eV; Stepanyuk et al. 1989) lies between the S 3*p* bonding orbitals in the VB and predominantly Ca 3*d* (and to a lesser extent Ca 4*s* σ*) antibonding orbitals in the CB (Kaneko and Koda 1988; Shameem Banu et al. 1998). In particular, the indirect band gap in CaS is bounded in the CB by low energy 3*d*-excited states of Ca, implying that the electron states of Ca are highly sensitive to adjustments in crystal potential (Shameem Banu et al. 1998); i.e., to change in stereochemical environment. In addition, the position of the metal 3*d* states relative to the metal 4*s* states in CaS results in a XANES spectrum with more similarities to that of the 3*d* transition metal-sulfides (i.e., MnS and FeS) than to MgS (see below).

Manganese has an experimental magnetism of 4.54 μ_B and a calculated magnetism of 4.92–4.59 μ_B (Fender et al. 1968; Freidman and Gubanov 1983; Hines et al. 1997). This supports the t_{2g}^3–e_g^2 electronic configuration, with the majority spin (↑) $t_{2g}\alpha$ and $e_g\alpha$ bands filled and minority spin (↓) t_{2g}^{β} and e_g^{β} bands empty. MnS is a diluted magnetic semiconductor and reportedly has outstanding magnetic and magneto-optical properties derived through interaction of hybridized S *sp* and Mn 3*d* states (Sato et al. 1997). At room temperature, α-MnS (Néel temperature, T_N ~152 K) has the antiferromagnetic spin-ordered type-II (AF_2) structure with the high-spin t_{2g}^3 and e_g^2 configuration (Tappero et al. 1997). α-MnS has insulating properties and the nature of the separation between the VB maximum and the CB minimum (i.e., the band gap) is controversial; e.g., it is given as ~2.7 eV in Sato et al. (1997), Tappero et al. (1997), and Hobbs and Hafner (1999), although literature estimates vary from as wide as 3.8 eV (Wang et al. 1996) to as narrow as 1.00 eV (calculated by Hobbs and Hafner 1999). The band gap in MnS lies between occupied Mn 3*d* states in the VB and unoccupied S 3*p* σ* antibonding states hybridized with Mn $3d(e_g)$ and $3d(t_{2g})$ σ* antibonding states in the CB (Huffman and Wild 1967; Freidman and Gubanov 1983).

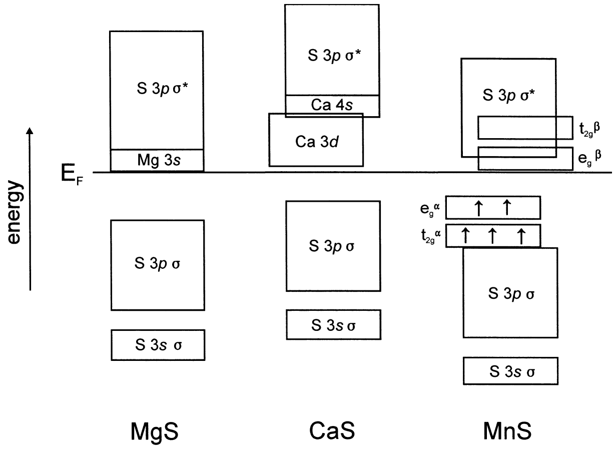

FIGURE 2. Schematic band structure models for MgS, CaS, and MnS emphasizing extensive hybridization of S 3*p* σ* antibonding and empty metal 3*d* states when available (i.e., CaS and MnS): E_F is Fermi level; see Figure 1 of Farrell and Fleet (2001) for band structure model of FeS (B8); band gap is 2.7 eV in MgS and 2.14 eV in CaS (Stepanyuk et al. 1992), and 2.7 eV in MnS (Freidman and Gubanov 1983).

Iron in FeS has the high spin t_{2g}^4–e_g^2 configuration with the majority spin (↑) $t_{2g}\alpha$ and $e_g\alpha$ bands filled, minority spin (↓) t_{2g}^{β} band one-third filled, and minority spin (↓) e_g^{β} band empty. This is confirmed by an experimental and calculated magnetism of 4.0 μ_B (Hobbs and Hafner 1999). The 3*d* electron configuration of divalent FeS with the NiAs-type structure is well understood from the magnetic behavior of this and related compounds (summarized in Table 3 of Hobbs and Hafner 1999) and is discussed in Farrell and Fleet (2001; cf. Fig. 2). Stoichiometric FeS is a small band gap (~0.1 eV) semiconductor and is antiferromagnetic at room temperature (RT; troilite), but the nature of the band gap and of the metallic behavior above 147 °C (where FeS is paramagnetic) is controversial (Marfunin 1979; King and Prewitt 1982; Sakkopoulos et al. 1984; Tossell and Vaughan 1992; Shimada et al. 1998). Electron delocalization through overlap of the partly filled t_{2g}^{β} and empty e_g^{β} bands is prohibited by symmetry. Goodenough (1967) recognized that trigonal distortion of the face-shared FeS_6 octahedra could split the t_{2g} levels below 147 °C into narrow bands parallel (Γ_I) and normal (Γ_{II}) to **c** and thus directly account for the energy gap; partial overlap of the Γ_I and Γ_{II} bands at the transition temperature would explain the metallic behavior at higher temperatures. The trigonal distortion of t_{2g}^{β} levels was retained symbolically in the schematic band structure model for FeS depicted in Figure 2 of Farrell and Fleet (2001).

RESULTS AND DISCUSSION

Powder X-ray diffraction

The powder X-ray diffraction (P-XRD) patterns of the monosulfide solid solutions (Table 1) are consistent with previous studies on the structure and phase transitions within the binary MgS-FeS, MgS-MnS, and MnS-FeS systems at 1000 °C and low pressure (Skinner and Luce 1971; Mann and Van Vlack 1976; McCammon et al. 1984). The *a* unit-cell parameters for end-member compositions are in good agreement with the corresponding JCPDS-ICDD card data; e.g., MgS (no. 35-0730; *a* = 5.200 Å), MnS (no. 06-0518; *a* = 5.224 Å), and FeS [no. 37-0477; *a* = 5.9676(7) Å and *c* = 11.761(3) Å]. Also, our value for CaS was 5.6953(4) Å, in good agreement with the JCPDS-ICDD card for synthetic oldhamite (no. 08-0464; *a* = 5.6948 Å). The extent of the $Mg_{1-x}Fe_xS$ (B1) solid solution is $x = 0.00–0.68$, and beyond 68 mol% FeS, $Mg_{0.32}Fe_{0.68}S$ (B1) coexists with FeS (B8). Phase relations in the $Mn_{1-x}Fe_xS$ system indicate an extensive alabandite (B1) solid solution over the interval $x = 0.00–0.74$ and a limited FeS (B8) solid solution at $x = 0.93–1.00$, separated by a two-phase region where $Mn_{0.26}Fe_{0.74}S$ (B1) coexists with $Fe_{0.93}Mn_{0.07}S$ (B8). Interestingly, stoichiometric FeS does not permit substitution of detectable concentrations of Mg for Fe, but will accept a significant amount (~7 mol% MnS) of Mn-for-Fe substitution. In agreement with Skinner and Luce (1971), there is complete miscibility in the MgS-MnS system.

The variation of the cubic (B1) unit-cell parameter (Table 1 and Fig. 1) over the compositions presently investigated is broadly consistent with data extrapolated from literature studies for the binary joins, for which dominant trends of near-linear increase in *a* cell edge length from FeS to MgS to MnS and FeS to MnS are well established and associated with change in electronic structure and bonding (Skinner and Luce 1971; McCammon et al. 1984; Osborne and Fleet 1984; Petrakovskii et al. 1999). With increase in substitution of Fe for Mg in $Mg_{1-x}Fe_xS$, the cubic unit cell is compressed with *a* decreasing from 5.2004(7) Å at $x = 0.00$ to 5.1204(3) Å at $x = 0.625$. Similarly, with increase in substitution of Fe for Mn in $Mn_{1-x}Fe_xS$, *a* decreases from 5.2233(5) Å at $x = 0.00$ to 5.0993(2)Å near $x = 0.75$. With increase in substitution of Mn for Mg in $Mg_{1-x}Mn_xS$, the cubic unit cell expands with *a* increasing from 5.2004(7) Å at $x = 0.00$ to 5.2233(5) Å at $x = 1.00$. Increase in substitution of Mn for Fe in troilite results in expansion of the troilite unit-cell; *a* and *c* are 5.9667(15) Å and 11.7516(29) Å for FeS and 6.033(20) Å and 11.763(39) Å at a bulk composition of $Fe_{0.875}Mn_{0.125}S$, respectively, consistent with the results of Skinner and Luce (1971). We also obtained a relatively high value for *c* [11.821(26) Å] in the bulk composition $Fe_{0.875}Mg_{0.125}S$, but did not investigate this potentially interesting effect further.

XANES spectra

Although the S *K*-edge XANES spectra were collected simultaneously in fluorescence yield (FY) and total electron yield (TEY) modes, more weight is presently given to the FY spectra because the FY signal is more representative of the bulk of the sample. The TEY signal preferentially samples the near surface and, therefore, may partly reflect near-surface modification resulting from alteration, contamination and, possibly, reconstruction (Farrell and Fleet 2001). These differences in spectra prove useful in some cases (e.g., near-surface studies), but are generally troublesome and may be eliminated provided samples are handled carefully (see Farrell and Fleet 2001). Since the cubic metal monosulfides are very susceptible to oxidative reaction and absorption of moisture during sample preparation, the extreme surface sensitivity of *L*-edge measurements may result in striking differences between spectra collected in the FY and TEY modes. Careful preparation of sample specimens for S *L*-edge studies, including the annealing of samples just prior to the XANES measurement, minimal grinding or other mechanical damage, and the use of an on-line nitrogen-filled glove bag, eliminated this problem in the present study. Corresponding TEY and FY S *L*-edge XANES spectra were essentially identical, so that the TEY spectra with superior signal-to-noise ratio properly represented the bulk samples. The spin-orbit coupling and greater resolution of spectral features make the S *L*-edge more sensitive to the local short-range bonding environment than the S *K*-edge. Although the XANES spectra of end-members and most intermediate compositions represent single phases, the XANES spectra of bulk compositions falling within two-phase regions represent the summation of the separate XANES features for each phase present (Table 1).

Sulfur *K*-edge. Sulfur *K*-edge FY-XANES spectra for (Mn,Fe)S and (Mg,Mn)S compositions are illustrated in Figures 3 and 4, and for (Mg,Fe)S compositions in Figure 2 of Farrell and Fleet (2000). The XANES spectra are characterized by a prominent edge feature b-c, and broad features d and e, which are presently attributed to multiple scattering resonances. In some cases, a pre-edge feature is present on the low-energy side of the edge peak, with variable intensity from a resolved peak (e.g., FeS) to a shoulder to the edge peak (e.g., MnS). The position of the pre-edge feature varies systematically with bulk composition from 2469.9 eV for FeS to 2471.0 eV for MnS, and 2473.8 eV for CaS; the pre-edge feature is absent from the MgS spectrum.

The edge feature b-c is attributed to transition of S 1*s* core level electrons to unoccupied S 3*p* σ* antibonding states. For the XANES spectrum of FeS, Womes et al. (1997) proposed that the features we label b and c may be due to transitions to unoccupied S 3*p* σ* antibonding states hybridized with Fe 4*s* σ* and Fe 4*p* σ* antibonding states, respectively, in the CB. Therefore, features b and c for the spectra of FeS and the other cubic monosulfides may be assigned similarly, when resolvable, and variation in their intensity represents fine-tuning in hybridization of the final states.

The pre-edge absorption features in metal *K*-edge XANES spectra of 3*d* transition-metal sulfides are attributed to transition of metal core electrons to unoccupied nonbonding 3*d* states. This transition, which is forbidden by the quantum selection rules in the electric dipole approximation ($\Delta L = \pm 1$), becomes weakly to strongly allowed in metal sulfides through hybrid-

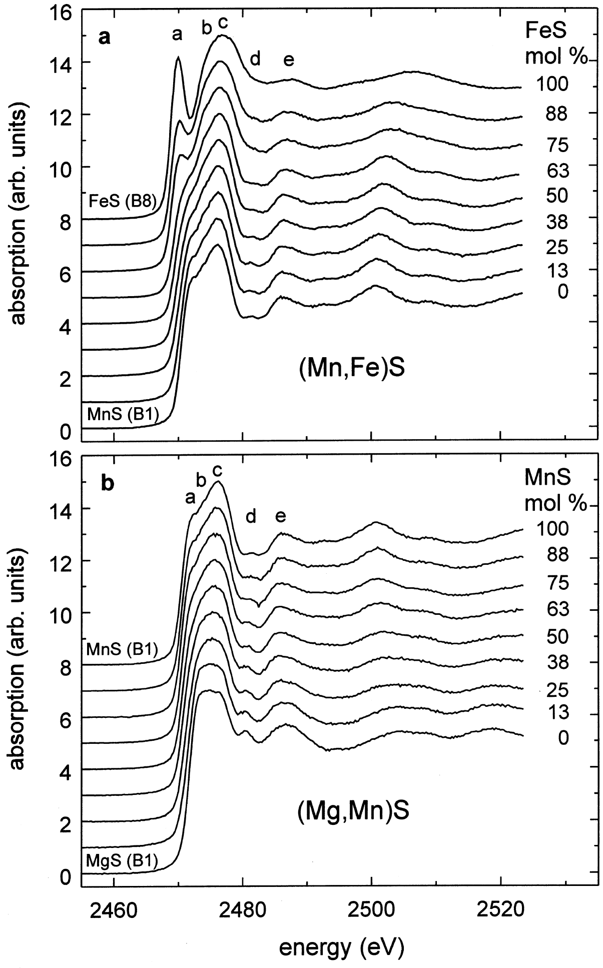

FIGURE 3. Sulfur *K*-edge FY-XANES spectra of: (**a**) (Mn,Fe)S, and (**b**) (Mg,Mn)S solid solutions arranged in upward sequence of progressively increasing average number of 3*d* electrons per metal atom. Note progressive evolution of the pre-peak feature a in each series; spectra are normalized to feature c and calibrated to the S *K*-edge of native S at 2472.0 eV.

ization of metal 3*d* states and S 3*p* σ* antibonding states (Tossell 1977). Therefore, the pre-edge feature in the S *K*-edge FY-XANES spectrum of FeS (troilite; B8; Figs. 3 and 4) has been assigned to transition of S 1*s* electrons to unoccupied hybridized S 3*p* σ* antibonding and Fe 3*d*(e_g) states (Farrell and Fleet 2000, 2001). In the derivative NiAs-type structure of FeS, these Fe 3*d*(e_g) orbitals have the appropriate symmetry for hybridization with S 3*p* σ* antibonding orbitals, while the Fe 3*d*(t_{2g}) orbitals do not. This hybridization implies that the main density of states (DOS) of S 3*p* and metal 3*d* orbitals above the Fermi level should be observable for all excitations involving anions of outermost S *p* states or final metal 3*d* states (Pong et al. 1997).

The S *K*-edge FY-XANES spectra of CaS and MnS are similar to that of FeS (Figs. 3 and 4), in that the pre-edge and edge features are attributable to transition of S 1*s* electrons to unoccupied hybridized S 3*p* σ* antibonding and metal 3*d*(e_g) states and unoccupied S 3*p* σ* antibonding states, respectively. Although Ca^{2+} is not a 3*d* transition-metal cation, CaS has the low-lying 3*d* behavior typical of the 3*d* cations (Fig. 2), so that a 3*d* orbital is still the lowest unoccupied orbital on the metal accessible to electrons. The S *K*-edge XANES spectrum of MgS does not show a pre-edge feature because there are no low-lying metal 3*d*(e_g) orbitals available to hybridize with S 3*p* σ* antibonding states at the bottom of the CB. The band structure of MgS (Fig. 2) is such that the band gap is bounded by low lying Mg 3*s* states at the bottom of the CB and the 3*d* states of Mg are too high in energy to hybridize with the S 3*p* σ* antibonding states. Therefore, the edge features b and c in the S *K*-edge FY-XANES spectrum of MgS (B1) have been assigned to transition of S 1*s* electrons to unoccupied hybridized S 3*p* σ* and Mg 3*s* σ* and Mg 3*p* σ* antibonding states, respectively.

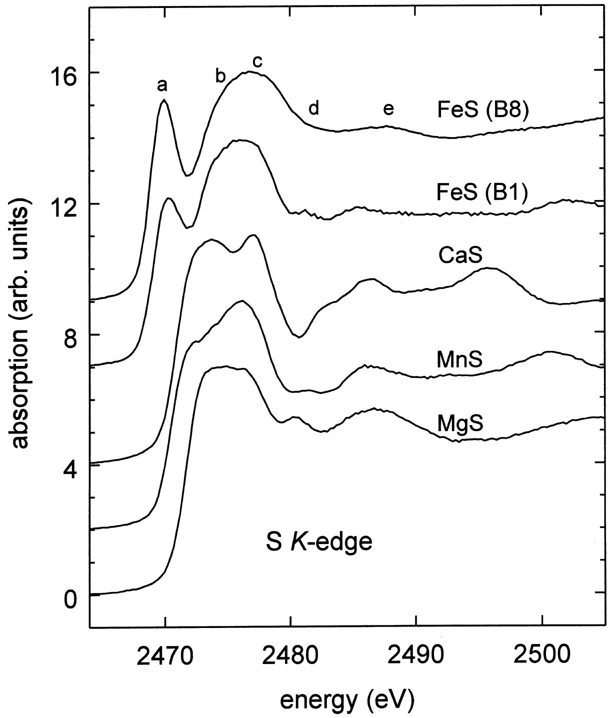

FIGURE 4. Sulfur *K*-edge FY-XANES spectra of FeS (troilite; derivative NiAs-type structure; B8) and rocksalt (B1) structure FeS (Farrell and Fleet 2000), CaS, MnS, and MgS; spectra are normalized to feature c and calibrated to the S *K*-edge of native S at 2472.0 eV.

The pre-edge feature a in the S *K*-edge FY-XANES spectra of rocksalt structure (octahedral) (Mg,Fe)S solid solutions was reported by Farrell and Fleet (2000) and assigned as discussed above. In addition, there have been several S *K*-edge XANES studies on tetrahedral $Zn_{1-x}Fe_xS$ mixed crystals with the zincblende (B3) structure (Li et al. 1994; Pong et al. 1994; Lawniczak-Jablonska et al. 1996) showing progressive evolution of a pre-edge feature assigned to transition of S 1*s* electrons to unoccupied hybridized S 3*p* and S 3*s* σ* antibonding and Fe 3*d*(t_2) states, although this was not noted in Li et al. (1994). Significantly, the intensity of the pre-edge shoulder increases progressively with increase in substitution by Fe in both the rocksalt and zincblende structures, clearly showing progressive increase in participation of Fe 3*d* orbitals in metal-S bonding.

Evolution of the pre-edge feature in the S *K*-edge XANES spectra of the present binary Fe-Mn-Mg monosulfide solid solutions (Fig. 3) is better resolved by subtracting the contribution to the S *K*-edge XANES spectrum of pure MgS, after normalizing to a common maximum height for the feature b-c, using BAN (Fig. 5). Because the energy-level diagram of MgS does not have low-lying 3*d* orbitals, these difference spectra should reveal the contribution of hybridized metal 3*d* electrons to the metal-S bonding of the solid solutions. The derived peak position and normalized area of the pre-edge feature for all compositions presently investigated are given in Table 1, and the variation in peak area with composition is plotted in Figure 6. It is evident that there is both a progressive increase in area and shift to lower energy of the pre-edge feature a with increase in Fe content for the (Mn,Fe)S solid solution and an increase in area at constant peak position with increase in Mn content for the (Mg,Mn)S solid solution. Similar trends in peak area and position were observed for binary MgS-FeS compositions in Farrell and Fleet (2000). Most importantly, it is noted that the area of the pre-edge feature does not change linearly from one end-member to another, showing that real changes in the band structure of the solid solutions are occurring. In other words, the S *K*-edge XANES spectra of, for example, (Mg,Mn)S solid solutions are not simply the weighted sum of local rocksalt-like end-member MnS and MgS clusters. Also note that the peak area distributions for (Mn,Fe)S and (Mg,Fe)S locate the position of the 1000 °C solvus for the corresponding rocksalt phase fairly precisely (cf. Skinner and Luce 1971).

The progressive increase in area of the pre-edge feature with increase in Fe and Mn contents is interpreted as an increase in overall compatibility of metal 3*d* states for hybridization with S 3*p* σ^* antibonding states, as proportionally more metal 3*d* orbitals become available in the sulfide structure. From comparison of the relative changes in the pre-edge feature for the three binary systems investigated and the intense pre-peak of FeS (B8: troilite; Figs. 3–6), it is evident that the pre-edge feature is also dependent on the type of host structure and substituting 3*d* cation. In chalcogenides with the rocksalt structure, the proportional increase in area of the pre-edge feature [or strength of S 3*p*-metal $3d(e_g)$ hybridization] is greatest for Fe substituting for Mg, intermediate for Fe substituting for Mn, and least for Mn substituting for Mg (Figs. 5 and 6). Thus, Fe^{2+} cations contribute 3*d* energy levels situated closest to the S 3*p* σ^* antibonding states and have a greater probability for hybridization with these states. The strength of *p-d* hybridization is reflected in the probability of an electronic transition occurring and as such varies as a function of the type and concentration of cation substituted. This shows that the size and position of the pre-edge feature are controlled more by the DOS of hybridized $3d(e_g^{\beta})$ states and nearest-neighbor coordination of the metal atoms, than by the precise coordination of S and the extended structure of the sulfide.

Progressive evolution of the pre-edge feature may also be correlated to increase in metallic character and an associated increase in covalence of the metal-S bond. Similarly, in the (Fe,Co,Ni) monosulfide solid solutions, pre-peak area, metallic character, and covalence increased in the sequence FeS to NiS to $Co_{1-x}S$, and was associated with an increase in the metal-metal bonding interaction and metal-sulfur π bonding (Farrell and Fleet 2001). In the present study, pre-edge peak area does not appear to correlate with change in unit-cell parameters (cf. Fig. 1). We speculate that MgS has a larger unit-cell volume than (Mg,Fe)S solid solutions due to the absence of 3*d* electrons in Mg-S bonding.

Sulfur *L*-edge. The complex nature and lack of interpretation for the S *L*-edge XANES spectra limits the assignment of individual features to those of the pre-edge (a_1 and a_2 in Fig. 7) and the edge itself (b_1 and b_2). All assignments of excitations for S *L*-edge XANES spectra of metal sulfides have emphasized the importance of hybridization of S and metal orbitals

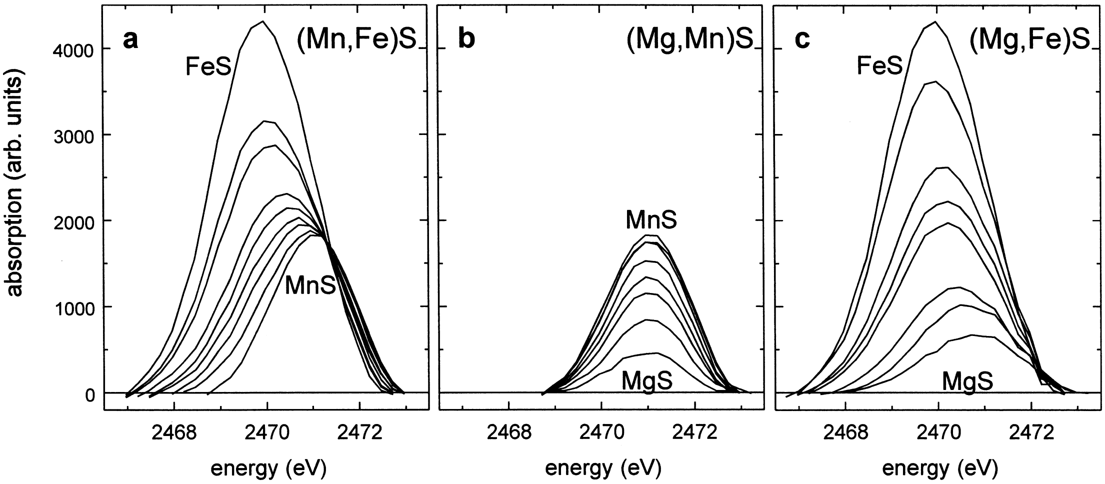

FIGURE 5. Pre-edge feature in the S *K*-edge FY-XANES spectra of: (**a**) (Mn,Fe)S, (**b**) (Mg,Mn)S, and (**c**) (Mg,Fe)S binary solid solutions isolated by subtraction of the spectrum of MgS. The pre-peak represents contributions from metal 3*d* orbitals, whereas the MgS spectrum is a good approximation of all other contributions to the edge region of the S *K*-edge XANES spectra of these metal sulfides.

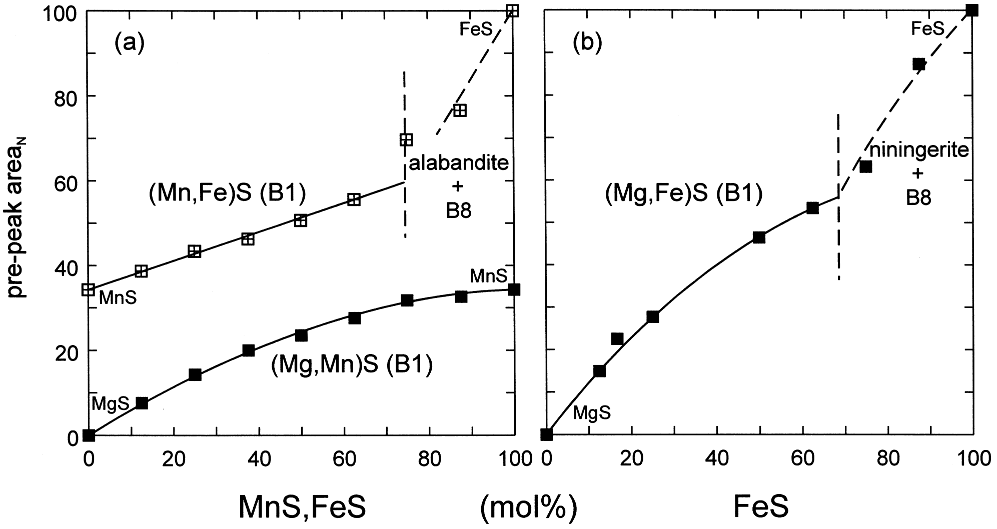

FIGURE 6. Variation in area of the pre-edge feature of S *K*-edge FY-XANES spectra with bulk composition for: (**a**) (Mn,Fe)S and (Mg,Mn)S, and (**b**) (Mg,Fe)S solid solutions (from Farrell and Fleet 2000). The smooth increase in pre-peak area with composition is interpreted to represent progressive increase in unoccupied metal $3d(e_g^{\beta})$ DOS, and the inflections indicate the phase boundaries (B1 phase solvus; dotted lines), in good agreement with P-XRD determinations (cf., Skinner and Luce 1971; McCammon et al. 1984).

(e.g., Chen 1997). The S *L*-edge is typically at ~162.5 eV and represents transition of S 2*p* core level electrons to unoccupied (or partially unoccupied) molecular orbital states (S 3*s* σ*, S 3*d*, S 4*s* σ*, etc.), as permitted by the quantum selection rules (Azároff 1968). In addition, the S *L* edge is split by 1.1–1.2 eV due to spin-orbit interaction of the two S 2*p* orbitals, S $2p_{3/2}$, and S $2p_{1/2}$; thus, peak b_1 represents the transition S $2p_{3/2}\rightarrow$S 3*s* σ* and b_2 the transition $2p_{1/2}\rightarrow$S 3*s* σ*, and these features correspond to the L_3- and L_2-edges, respectively. This spin-orbit splitting is clearly evident in the spectrum of native S and has been identified also in the XANES spectra of MgS, CaS, and MnS (Fig. 7). The paired features f_1 and f_2 resolved in the XANES spectra of native S and CaS (Fig. 7) are presently attributed to either an "echo" or shadow effect of the spin-orbit split S *L*-edge features due to multiple scattering or transition to localized levels higher up the conduction band. The pre-edge features a_1 and a_2 represent transition of S $2p_{3/2}$ and S $2p_{1/2}$ electrons to S 3*s* σ* states hybridized with metal $3d(e_g + t_{2g})$ and $3d(e_g)$ states, respectively. In the S *L*-edge XANES spectrum of FeS, the pre-edge feature is dominant over the edge feature due to the strong hybridization of S 3*s* σ* and Fe $3d(e_g)$ states (a_2) and weak π-bonds associated with the hybridization of S 3*s* σ* and Fe $3d(t_{2g})$ (a_1). The pre-edge features also appear to be strong in the XANES spectrum of CaS, which we attribute to hybridization with empty Ca 3*d* and S 3*d* states at the bottom of the CB (Fig. 2). Other features in the S *L*-edge XANES spectra are likely associated with multiple scattering resonances and have been identified with numerical labels. These assignments and labels differ in detail from Li et al. (1994, 1995) who placed more emphasis on crystal field splitting of Fe 3*d* states.

Comparison of S *K*- and *L*-edge XANES features indicates that, due to the extensive hybridization of S and metal orbitals, the final states should be equivalent. Importantly, the main exception is the transition to the mixed metal 3*d* (t_{2g} and e_g) states, which occurs at the S *L*-edge (a_1 in Figs. 7 and 8) but not at the

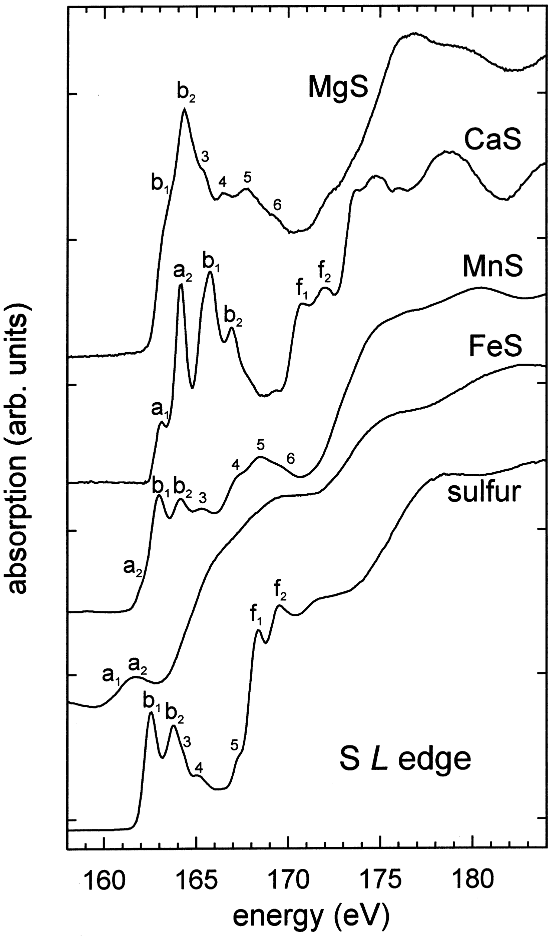

FIGURE 7. Sulfur *L*-edge TEY-XANES spectra of rocksalt (B1) structure MgS, CaS and MnS, NiAs-type structure (B8) FeS, and native sulfur; spectra are calibrated to the S L_3-edge ($2p_{3/2}$) of native S at 162.5 eV.

S *K*-edge. This transition, while allowed at the *L*-edge due to overlap of S 3*s* σ* and metal 3*d*(t_{2g}) orbitals, is symmetry forbidden at the *K*-edge: the geometry of the 3*d*(t_{2g}) orbitals excludes extensive hybridization with the S 3*p* σ* antibonding states (Azároff 1968).

The S *L*-edge XANES spectra of the (Mn,Fe)S, (Mg,Mn)S, and (Mg,Fe)S solid solutions (Fig. 8) show progressive change consistent with that reported above for the S *K*-edge XANES spectra. However, the greater complexity of the S *L*-edge spectra and lack of reproducibility of the background does not permit quantitative analysis similar to that achieved for the S *K*-edge spectra (Figs. 5 and 6). The *L*-edge features at each intermediate composition reflect progressive change in the electronic band structure of the solid solutions and are not simply the sum of the combined features of the end-member compositions. This is readily apparent by comparison of the S *L*-edge spectra of rock salt structure $Mg_{0.5}Fe_{0.5}S$, $Mg_{0.5}Mn_{0.5}S$, and $Mn_{0.5}Fe_{0.5}S$, with corresponding summed spectra calculated by linear combination of the relevant end-members (Fig. 9). It is clear that the summed spectra are very different from the actual XANES spectra.

The S *L*-edge XANES spectra of the solid solutions confirm our assignments of the edge feature (b_1, b_2) for MgS (Fig. 8b), the weak edge feature in FeS (troilite; B8) and FeS-rich compositions (Fig. 8a,c), and the pre-edge feature (a_1, a_2). The evolution of the pre-edge feature may be the most interesting result. Although a_2 is dominant in end-member FeS, both a_1 and a_2 are clearly resolved in (Mn,Fe)S and (Mg,Fe)S solid solutions, with a_1 becoming dominant with increase in Mn and Mg contents, respectively (or decrease in Fe content). Also, both a_1 and a_2 disappear at (or before) the MnS and MgS end-member compositions. Since the a_1 feature has been attributed to transitions of S $2p_{3/2}$ electrons to S 3*s* σ* states hybridized with metal 3*d*(e_g and t_{2g}) states, this may represent a relative increase in strength of metal-S π-bonding in the Mn- and Mg-rich solid solutions. Also, in Mn-rich compositions, the weak low-energy shoulder to the edge feature in the spectrum of MnS, which we have identified as a pre-edge feature and which is equivalent to the pre-edge feature in the *K*-edge XANES spectrum of MnS (Fig. 3), remains distinct from the pre-edge feature associated with the Fe atoms. This is direct evidence for localized Mn and Fe states in these mixed crystals.

Computer simulation

It is now accepted that the XANES region above the *K*-edge for solid matter is generated by multiple scattering of the excited photoelectron within a large cluster consisting of a few shells of atoms. The algorithm for the full multiple scattering method used in this theoretical study has been described earlier (Durham et al. 1982). The G4XANES program (Della Longa et al. 1995) calculates the angular momentum of selected transition probabilities to occupied and unoccupied electronic states beyond the intersphere potential (V_{MT}). In particular, for simulation of S *K*-edge spectra, the probability of electron transitions from the S 1*s* ($l = 0$, $m_L = 0$) core level to delocalized final states of *p*-symmetry ($l = 1$, $m_L = 0,1$) are calculated.

Within the dipole approximation, the X-ray absorption coefficient (μ) for the S *K*-edge is proportional to both the partial density of unoccupied S *p*-symmetry states and the squared dipole transition matrix element, i.e.;

$$\mu = |m_L(E)|^2 N_p^S(E) \qquad (1)$$

where $N_p^S(E)$ is the partial density of unoccupied S *p*-symme-

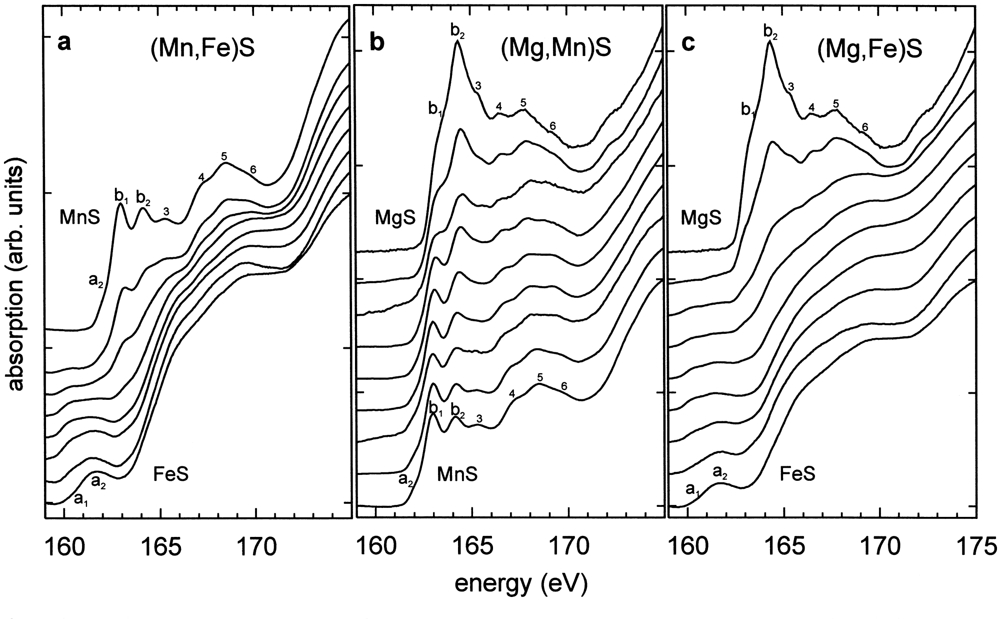

FIGURE 8. Sulfur *L*-edge TEY-XANES spectra of: (**a**) (Mn,Fe)S, (**b**) (Mg,Mn)S, and (**c**) (Mg,Fe)S solid solutions arranged in downward sequence of progressively increasing average number of 3*d* electrons per metal atom. Note progressive evolution of the edge (b_1 and b_2) and pre-edge (a_1 and a_2) features; spectra are normalized to the envelope at 175 eV and calibrated to the S L_3-edge ($2p_{3/2}$) of native S at 162.5 eV.

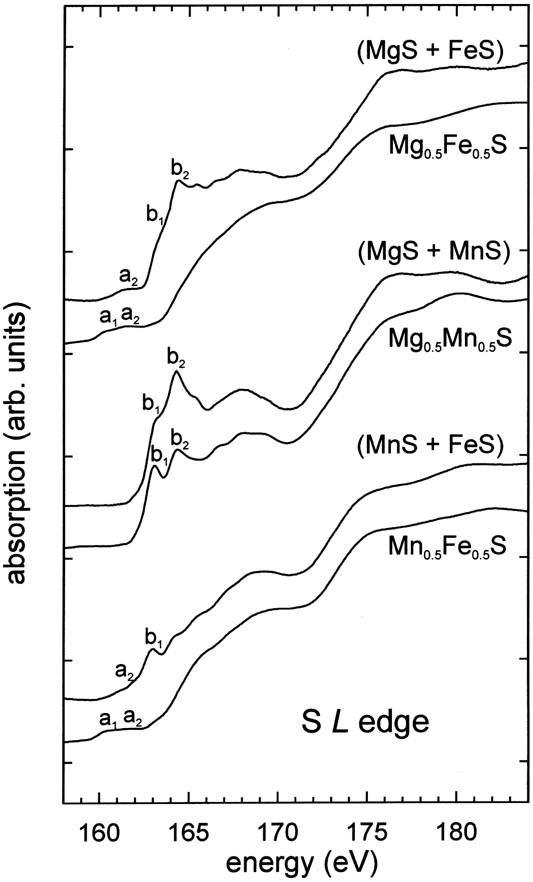

FIGURE 9. Sulfur *L*-edge TEY-XANES spectra of rocksalt (B1) structure $Mg_{0.5}Fe_{0.5}S$, $Mg_{0.5}Mn_{0.5}S$ and $Mn_{0.5}Fe_{0.5}S$, compared with corresponding summed spectra calculated by linear combination of the relevant end-members (e.g, 0.5MgS + 0.5FeS for $Mg_{0.5}Fe_{0.5}S$, etc.). Note that *L*-edge features are representative of the electronic band structure at each composition and are not simply a sum of the combined features of the end-member compositions; spectra are calibrated to the S L_3-edge ($2p_{3/2}$) of native S at 162.5 eV.

try states, and $m_L(E)$;

$$m_L(E) = [\int dr\ \psi(r,E)(r)\Phi_c(r)]\ /\ [\{\int dr\ \Psi(r,E)^2\}^{1/2}] \tag{2}$$

is the normalized dipole transition matrix element, where $\psi(r,E)$ is the solution of the radial Schrodinger equation at energy E for the muffin-tin potential ($l = 1$ for the *K*-edge), (r) is the electron-photon interaction operator and $\Phi_c(r)$ is the core *K*-level wave function for sulfur. Therefore, in practice, the program calculates $E \parallel z$ ($m_L = 0$) and $E \parallel xy$ ($m_L = 1$) polarized XANES spectra; the unpolarized spectrum is obtained by a 2:1 weighted sum of the $E \parallel xy$ and $E \parallel z$ spectra.

For the present rocksalt (B1) structure sulfides, phase shifts were included, with orbital momentum up to 3 because there is almost no change in the spectra in comparison with $l = 2$ (Table 2). Phase shifts were calculated in the crystal muffin-tin (MT) potential with touching MT spheres. The muffin-tin radii and the muffin-tin constants obtained according to the procedure for the muffin-tin potential construction are reported in Table 2. The muffin-tin approximation used was based on the Mattheiss (1969) prescription with an exchange parameter equal to 1.0 while constructing the crystal potential. Atomic charge densities were obtained with the help of the self-consistent Dirac-Slater method.

The first step in the multiple scattering analysis of XANES data is to determine the size of a representative cluster of neighboring atoms around the absorbing S atom that will fully reproduce all of the fine structure of unoccupied electronic states in the conduction band of the sulfides. XANES calculations using different cluster sizes (i.e., 1, 3, 5, and 9 shells) are used to show convergence with experimental FY-XANES spectra for MgS, MnS, and CaS (Fig. 10). As shown in Figure 10, analysis of the dependence of the main features in the XANES spectra on cluster size shows convergence for a cluster with 5 shells for MnS and with 9 shells for MgS and CaS (addition of further shells results in no significant change to the calculated spectra).

Another factor, beyond phase shifts and local cluster structure, that determines the XANES features in the multiple scattering formalism is the transition matrix element (Eq. 2), which influences the relative intensity of XANES features. The S *K*-edge X-ray absorption, in the dipole approximation, has been shown to be proportional to the partial density of unoccupied S *p*-states in the conduction band of the sulfides. Therefore, if the coefficient of proportionality, namely the dipole matrix element (Eq. 2), is not a very sharp function of energy, as it is in the present case in the energy interval above 10 eV, one can, to a first approximation, study the details of the partial DOS, averaged in real space, by analyzing the fine structure of the X-ray absorption spectra. Figure 10 shows a representation of the squared dipole transition matrix element $|m_L(E)|^2$ as a function of energy for the ground state potential for all compounds under investigation. Thus, in the energy interval close to the absorption threshold the squared dipole transition matrix element shows an energy independence (especially ~10 eV above the main edge) and can be treated as a constant.

To perform the direct comparison with experimental data two factors must be taken into account; the filling of occupied states following the Fermi distribution and the broadening of experimental spectra. This broadening is dependent on the core hole lifetime, the finite mean free path of the photoelectron, and the experimental resolution. For the *K* core hole bandwidth the value of 0.59 eV (Fuggle and Inglesfield 1992) was used, the mean free path of the photoelectron was taken from the

TABLE 2. Unit-cell parameters, muffin-tin radii (R_{mt}) and constants (V_o) used for the muffin-tin approximation after Mattheiss (1969)

Compound	Unit-cell parameters (Å)	Muffin-tin parameters		
		atom	R_{mt} (Å)	V_o (eV)
MgS (B1)	a = 5.203	Mg	1.2175	−14.44
		S	1.3731	−14.67
FeS (B8)	a = 3.438	Fe	1.4051	−11.83
	c = 5.880	S	1.4277	−11.46
FeS (B1)	a = 5.074	Fe	1.2815	−16.05
		S	1.2502	−15.77
MnS (B1)	a = 5.224			
CaS (B1)	a = 5.690			

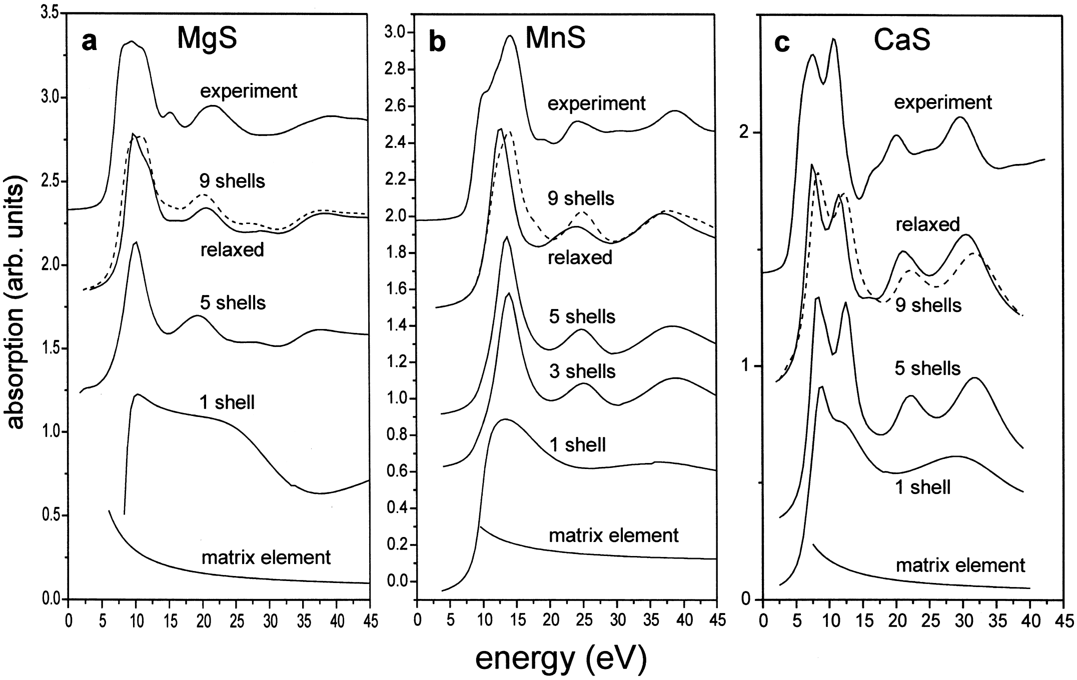

FIGURE 10. Experimental and theoretical S *K*-edge XANES spectra of (**a**) MgS, (**b**) MnS, and (**c**) CaS. The theoretical spectra were calculated taking into account all of the broadening factors and the Fermi distribution, and the relaxed spectrum (dashed line) was calculated in the Z + 1 approximation.

energy dependent function obtained by Muller et al. (1982), and the value for the experimental energy resolution was chosen as 0.5 eV. We treated all of these factors as contributing to the imaginary part of the self-energy term that was used.

Comparison of theory and experiment

The agreement between the theoretical and experimental S *K*-edge XANES spectra improves, as would be expected, with expansion of the cluster size (Fig. 10). Strictly speaking one must compare the experimental spectrum with the theoretical calculation made in relaxed potential (i.e., taking into account the presence of the core hole created by the electronic transition). This is conventionally treated using the Z + 1 approximation (Bianconi 1989). The theoretical S *K*-edge XANES calculated in both the ground state (unrelaxed) and the Z + 1 (fully relaxed) approximation do not differ significantly (especially when broadening factors are taken into account; Fig. 10). Small differences in relative intensity arise from the difference in the dipole transition matrix elements calculated in the unrelaxed and the fully relaxed potentials. Although the contribution of the core hole effect at the S *K*-edge is rather small, it becomes significant at the L_3- and L_2-edges (Soldatov 1993a, 1993b 1994). In general, the present theoretical method works best for crystal structures of cubic symmetry. For example, for the B1-type MgS, CaS, and MnS compounds, there is a good correlation between the theoretical and corresponding experimental spectra, but for the hexagonal B8 structure of FeS, the agreement is less satisfactory (Stekhin et al. 2001). The present theory does successfully reproduce the splitting of the S *K*-edge of CaS, which we have assigned to transition to empty Ca 3*d* states hybridized with S 3*p* σ* antibonding states (Fig. 2), and the pre-edge of FeS (B8; Stekhin et al. 2001) but is somewhat less successful for the pre-edge of MnS (Fig. 10) and of the experimentally derived XANES spectrum of FeS (B1; Stekhin et al. 2001). Nevertheless, pre-edge features are often neglected in theoretical studies, so these results must be viewed as a positive step forward.

ACKNOWLEDGMENTS

We thank G. Retzlaff and K. Tan, Canadian Synchrotron Radiation Facility, and staff of the Synchrotron Radiation Centre (SRC), University of Wisconsin-Madison, for their technical assistance, the National Science Foundation (NSF) for support of the SRC under the grant no. DMR-0084402, and Kim Law for assistance with P-XRD. This work was supported by the Natural Sciences and Engineering Research Council of Canada.

REFERENCES CITED

Azároff, L.V. (1968) Elements of X-ray Crystallography, 610 p. McGraw-Hill Inc., New York.

Bancroft, G.M. (1992) New developments in far UV, soft X-ray research at the Canadian Synchrotron Radiation Facility. Canadian Chemical News, 44, 15–22.

Bianconi, A. (1989) XANES Spectroscopy. In D.C. Koningsberger and R. Prins, Eds., X-ray Absorption: Principles, Applications and Techniques of EXAFS, SEXAFS and XANES, p. 573–662. Chemical Analysis, 92, Wiley, New York.

Chen, J.G. (1997) NEXAFS investigations of transition metal oxides, nitrides, carbides, sulfides and interstitial compounds. Surface Science Reports, 30, 1–152.

Della Longa, S., Soldatov, A., Pompa, M., and Bianconi, A. (1995) Atomic and electronic structure probed by X-ray absorption spectroscopy: full multiple scattering analysis with the G4XANES package. Computational Materials Science, 4, 199–210.

Durham, P.J., Pendry, J.B., and Hodges, C.H. (1982) Calculation of X-ray absorption near-edge structure, XANES. Computer Physics Communications, 25, 193–205.

Farrell, S.P. and Fleet, M.E. (2000) Evolution of local electronic structure in cubic Mg$_{1-x}$Fe$_x$S by S *K*-edge XANES spectroscopy. Solid State Communications, 113, 69–72.

———(2001) Sulfur *K*-edge XANES study of local electronic structure in ternary monosulfide solid solution [(Fe, Co, Ni)$_{0.923}$S]. Physics and Chemistry of Minerals, 28, 17–27.

Fender, B.E.F., Jacobson, A.J., and Wedgwood, F.A. (1968) Covalency parameters in MnO, α-MnS, and NiO. Journal of Chemical Physics, 48, 990–994.

Fleet, M.E. and MacRae, N.D. (1987) Sulfidation of Mg-rich olivine and the stability of niningerite in enstatite chondrites. Geochimica et Cosmochimica Acta, 51, 1511–1521.

Freidman, S.P. and Gubanov, V.A. (1983) Electronic structure of *3d*-metal monosulphides by the *X*α discrete vibrational method. Journal of Physics and Chemistry of Solids, 44, 187–194.

Frondel, J.W. (1975) Lunar Mineralogy. Wiley, New York.

Fuggle, J.C. and Inglesfield, J.E., Eds., (1992) Unoccupied electronic states: Fundamentals for XANES, EELS, IPS and BIS, 360 p. Topics in Applied Physics, 69, Springer-Verlag, New York.

Goodenough, J.B. (1967) Description of transition metal compounds: application to several sulfides. In Propértés Thermodynamiques Physiques et Structurales des Dérivés Semi-metalliques, p. 263–292. Centre National de la Recherche Scientifique, Paris.

Goodrich, C.A. and Delaney, J.S. (2000) Fe/Mg-Fe/Mn relations of meteorites and primary heterogeneity of primitive achondrite parent bodies. Geochimica et Cosmochimica Acta, 64, 149–160.

Hines, R.I., Allan, N.L., Bell, G.S., and Mackrodt, W.C. (1997) An *ab initio* Hartree-Fock study of the magnetic states of the polymorphs of MnS. Journal of Physics: Condensed Matter, 9, 7105–7118.

Hobbs, D. and Hafner, J. (1999) Magnetism and magneto-structural effects in transition-metal sulphides. Journal of Physics: Condensed Matter, 11, 8197–8222.

Huffman, D.R. and Wild, R.L. (1967) Optical properties of α-MnS. Physical Review, 156, 989–997.

Kalpana, G., Palanivel, B., Thomas, R.M., and Rajagopalan, M. (1996) Electronic and structural properties of MgS and MgSe. Physica, B222, 223–228.

Kaneko, Y. and Koda, T. (1988) New developments in IIa-VIb (alkaline-earth chalcogenide) binary semiconductors. Journal of Crystal Growth, 86, 72–78.

Kasrai, M., Lennard, W.N., Brunner, R.W., Bancroft, G.M., Bardwell, J.A., and Tan, K.H. (1996) Sampling depth of total electron yield and fluorescence measurements in Si L- and K-edge absorption spectroscopy. Applied Surface Science, 99, 303–312.

Kawai, J., Adachi, H., Hayakawa, S., Zhen, S.Y., Kobayashi, K., Gohshi, Y., Maeda, K., and Kitajima, Y. (1994) Depth selective X-ray absorption fine structure spectrometry. Spectrochimica Acta, 49B, 739–743.

King, H.E. Jr. and Prewitt, C.T. (1982) High-pressure and high-temperature polymorphism of iron sulfide (FeS). Acta Crystallographica, B38, 1877–1887.

Kitamura, M., Sugiura, C., and Muramatsu, S. (1988) Multiple-scattering calculation of sulfur K X-ray absorption spectra for FeS, CoS and NiS. Solid State Communication, 67, 313–316.

Ławniczak-Jabłonska, K., Iwanowski, R.J., Gołacki, Z., Traverse, A., Pizzini, S., Fontaine, A., Winter, I., and Hormes, J. (1996) Local electronic structure of ZnS and ZnSe doped by Mn, Fe, Co, and Ni from x-ray-absorption near-edge structure studies. Physical Review B, 53, 1119–1128.

Li, D., Bancroft, G.M., Kasrai, M., Fleet, M.E., Yang, B.X., Feng, X.H., Tan, K, and Peng, M. (1994) Sulfur K- and L-edge x-ray absorption spectroscopy of sphalerite, chalcopyrite and stannite. Physics and Chemistry of Minerals, 20, 489–499.

Li, D., Bancroft, G.M., Kasrai, M., Fleet, M.E., Feng, X., and Tan, K. (1995) S *K*- and *L*-edge X-ray absorption spectroscopy of metal sulfides and sulfates: applications in mineralogy and geochemistry. Canadian Mineralogist, 33, 949–960.

Lichanot, A., Dargelos, A., Larrieu, C., and Orlando, R. (1994) Electronic structure and phase transition in magnesium sulphide. Solid State Communications, 90, 189–193.

Mann, G.S. and Van Vlack, L.H. (1976) FeS-MnS phase relationships in the presence of excess iron. Metallurgical Transactions, 7B, 469–475.

Marfunin, A.S. (1979) Physics of Minerals and Inorganic Compounds. Springer-Verlag, New York, 340 p.

Mattheiss, L.F. (1969) Band structure and fermi surface of ReO_3. Physical Review, 181, 987–1000.

McCammon, C.A., Jackson, I., Ringwood, A.E., and Cashion, J.D. (1984) The binary systems FeS-MgS and FeS-MnS: Mössbauer spectroscopy of the B1 solid solutions and high-pressure phase equilibria. Physics and Chemistry of Minerals, 11, 182–193.

Müller, J.E., Jepsen, O., and Wilkins, J.W. (1982) X-ray absorption spectra: L-edges of 3d transition metals, L-edges of 3d and 4d metals, and M-edges of palladium. Solid State Communications, 42, 365–368.

Osborne, M.D. and Fleet, M.E. (1984) Mössbauer investigation of niningerite solid solutions (Mg,Fe)S. Physics and Chemistry of Minerals, 10, 245-249.

Petrakovskiĭ, G.A., Ryabinkina, L.I., Kiselev, N.I., Velikanov, D.A., Bovina, A.F., and Abramova, G.M. (1999) Colossal magnetoresistance of $Fe_xMn_{1-x}S$ magnetic semiconductors. JEPT Letters, 69, 949–953.

Pong, W.F., Mayanovic, R.A., Wu, K.T., Tseng, P.K., Bunker, B.A., Hiraya, A., and Watanabe, M. (1994) Influence of transition-metal type and content on local-order properties of $Zn_{1-x}M_xS$ (M=Mn,Fe,Co) alloys studied using XANES spectroscopy. Physical Review B, 50, 7371–7377.

Pong, W.F., Mayanovic, R.A., Kao, J.K., Hsieh, H.H., Pieh, J.Y., Chang, Y.K., Kuo, K.C., Tseng, P.K., and Lee, J.F. (1997) Degree of *p-d* hybridization in $Zn_{1-x}Mn_xY$ (Y=S,Se) and $Zn_{1-x}Co_xS$ alloys as studied by x-ray-absorption spectroscopy. Physical Review B, 55, 7633–7640.

Sakkopoulos, S., Vitoratos, E., and Argyreas, T. (1984) Energy-band diagram for pyrrhotite. Journal of Physics and Chemistry of Solids, 45, 923–928.

Sato, H., Mihara, T., Furuta, A., Tamura, M., Mimura, K., Happo, N., Taniguchi, M., and Ueda, Y. (1997) Chemical trend of occupied and unoccupied Mn 3*d* states in MnY (Y=S, Se,Te). Physical Review B, 56, 7222–7231.

Shameem Banu, I.B., Kalpana, G., Palanivel, B., Shenbagaraman, P., Rajagopalan, M., and Yousuf, M. (1998) *Ab Initio* electronic band structure calculations for calcium monochalcogenides. International Journal of Modern Physics B, 12, 1709–1717.

Shimada, K., Mizokawa, T., Mamiya, K., Saitoh, T., Fujimori, A., Ono, K., Kakizaki, A., Ishii, T., Shirai, M., and Kamimura, T. (1998) Spin-integrated and spin-resolved photoemission study of Fe chalcogenides. Physical Review B, 57, 8845–8853.

Skinner, B.J. and Luce, F.D. (1971) Solid solutions of the type (Ca,Mg,Mn,Fe)S and their use as geothermometers for the enstatite chondrites. American Mineralogist, 56, 1269–1296.

Soldatov, A.V., Della Longa, S., and Bianconi, A. (1993a) Relevant role of hydrogen atoms in the XANES of Pd hydride: Evidence of hydrogen induced unoccupied states. Solid State Communications, 85, 863–868.

Soldatov, A.V., Ivanchenko, T.S., Stekhin, I.E., and Bianconi, A. (1993b) X-ray absorption fine-structure investigation of the ionic compounds NaBr, KBr and RbCl: Full multiple-scattering analysis. Journal of Physics: Condensed Matter, 5, 7521–7528.

Soldatov, A.V., Ivanchenko, T.S., Della Longa, S., Kotani, A., Iwamoto, Y., and Bianconi, A. (1994) Crystal-structure effects in the Ce L_3 -edge x-ray-absorption spectrum of CeO_2: Multiple-scattering resonances and many-body final states. Physical Review B, 50, 5074—5080.

Stekhin, I.E., Soldatov, A.V., Farrell, S.P., and Fleet, M.E. (2001) Electronic structure investigation of $Mg_{1-x}Fe_xS$ solid solution: X-ray absorption study. Journal of Synchrotron Radiation, 8, 238–239.

Stepanyuk, V.S., Szász, A., Farberovich, O.V., Grigorenko, A.A., Kozlov, A.V., and Mikhailin, V.V. (1989) An electronic band structure calculation and the optical properties of alkaline-earth sulphides. Physica Status Solidi B, 155, 215–220.

Stepanyuk, V.S., Grigorenko, A.A., Katsnelson, A.A., Farberovich, O.V., Szász, A., and Mikhailin, V.V. (1992) Electronic structure and optical properties of MgS. Physica Status Solidi B, 174, 289–294.

Stöhr, J. (1988) In X-ray Absorption: Principles, Applications and Techniques of EXAFS, SEXAFS and XANES (D.C. Koningsberger and R. Prins, Eds.), 573–662. Chemical Analysis 92, John Wiley & Sons, New York.

Sugiura, C. and Muramatsu, S. (1985) Sulfur K X-ray absorption-edge structures and electronic states of transition-metal sulfides MS and MS_2 (M = Fe, Co, Ni). Physica Status Solidi B, 129, K157–K161.

Tan, K.H., Bancroft, G.M., Coatsworth, L.L., and Yates, B.W. (1982) Mark IV "Grasshopper" grazing incidence monochromator for the Canadian Synchrotron Radiation Facility (CSRF). Canadian Journal of Physics, 60, 131–136.

Tappero, R., D'Arco, P., and Lichanot, A. (1997) Electronic structure of □-MnS (alabandite): an ab initio study. Chemical Physics Letters, 273, 83–90.

Tossell, J.A. (1977) SCF-$X_{□}$ scattered wave MO studies of the electronic structure of ferrous iron in octahedral coordination with sulfur. Journal of Chemical Physics, 66, 5712–5719.

Tossell, J.A. and Vaughan, D.J. (1992) Theoretical Geochemistry: Applications of Quantum Mechanics in the Earth and Mineral Sciences. Oxford University Press, New York.

Tyliszczak, T. (1992) BAN Data Analysis Program. McMaster University.

Wang, L., Sivanathan, S., Sporken, R., and Caudano, R. (1996) Interface properties and valence-band discontinuity of MnS/ZnSe heterostructures. Physical Review B, 54, 2718–2722.

Weast, R.C., Astle, M.J., and Beyer, W.H., Eds. (1986) CRC Handbook of Chemistry and Physics, 67th edition, p. F166. CRC Press Inc., Boca Raton, Florida.

Womes, M., Karnatak, R.C., Esteva, J.M., Lefebvre, I., Allan, G., Olivier-Fourcade, J., and Jumas, J.C. (1997) Electronic structures of FeS and FeS_2: X-ray absorption spectroscopy and band structure calculations. Journal of Physics and Chemistry of Solids, 58, 345–352.

Yang, B.X., Middleton, F.H., Olsson, B.G., Bancroft, G.M., Chen, J.M., Sham, T.K.,Tan, K., and Wallace, D.J. (1992) The design and performance of a soft X-ray double crystal monochromator beamline at Aladdin. Nuclear Instruments and Methods in Physics Research A, 316, 422–436.

MANUSCRIPT RECEIVED JULY 10, 2001
MANUSCRIPT ACCEPTED MAY 11, 2002
MANUSCRIPT HANDLED BY JAMES KUBICKI

View publication stats